Journal of Materials Chemistry A

ROYAL SOCIETY OF CHEMISTRY

PAPER

View Article Online
View Journal | View Issue

Cite this: J. Mater. Chem. A, 2024, 12, 2359

Two-dimensional trilayer heterostructures with cascade dual Z-schemes to achieve efficient hydrogen evolution reaction†

Xue-Qing Wan, [a] Chuan-Lu Yang, *[ab] Xiao-Hu Li, [bc] Yu-Liang Liu [a] and Wen-Kai Zhao [a]

Cascade dual Z-schemes for photocatalytic overall water splitting for hydrogen production are constructed for trilayer Bi/HfSeTe/$ZrSe_2$, Bi/HfSeTe/$ZrSe_2$, and $InAs_3$/HfSeTe/$ZrSe_2$ heterostructures. Electronic properties are studied by first-principles calculations, and the photoexcited carrier pathway is explored by nonadiabatic molecular dynamics simulations. The arrow-up, arrow-down, and cascade arrangement of band alignments for the Bi/HfSeTe/$ZrSe_2$ and $InAs_3$/HfSeTe/$ZrSe_2$ heterostructures are explored, and those for the $HfSe_2$/$ZrSe_2$/$HfSe_2$ and $ZrSe_2$/$HfSe_2$/$ZrSe_2$ sandwich heterostructures are also considered for comparison. The solar-to-hydrogen efficiency of 22.08% for the bilayer HfSeTe/$ZrSe_2$ heterostructure can be raised to 40.52%, 39.47%, and 41.04% by the cascade dual Z-schemes with Bi/HfSeTe/$ZrSe_2$, Bi/HfSeTe/$ZrSe_2$, and $InAs_3$/HfSeTe/$ZrSe_2$. They can further be boosted to 41.53%, 41.12%, and 43.57% under 1%, 1%, and −2% biaxial strains, respectively. The nonadiabatic molecular dynamics simulations reveal that the activity of the photogenerated carriers can be well protected. Moreover, the Gibbs free energy changes demonstrated that the hydrogen and oxygen evolution reactions driven by Bi/HfSeTe/$ZrSe_2$ can spontaneously proceed. Therefore, the cascade dual Z-scheme provides an effective way to develop highly efficient photocatalysts for hydrogen generation from overall water splitting.

Received 5th November 2023
Accepted 15th December 2023

DOI: 10.1039/d3ta06755f

rsc.li/materials-a

1. Introduction

Serious environmental and energy problems have arisen with the rapid economic development of countries around the world.[1] The method of photocatalytic water splitting to produce hydrogen is gaining considerable attention due to its advantages of being inexpensive and non-polluting.[2] Photocatalyst performance is promoted by a high carrier separation efficiency, wide light absorption range, and strong redox ability.[3] Extensive efforts have been devoted to improving the photocatalytic ability of materials by enhancing the above factors. For example, constructing Janus monolayers with electrostatic potential difference ($\Delta\varphi$) on two surfaces is one of the most effective methods of facilitating internal carrier separation,[4–6] such as group III chalcogenides,[7] III_2–VI_3 groups,[8] and group VI chalcogenides.[9] Establishing heterostructures also has the above advantages and can further improve the overpotential of the hydrogen evolution reaction (HER) and oxygen evolution reaction (OER) compared with the monolayers composing them.[10,11] Bilayer heterostructures can be classified into three types according to their different band structures. Type-I heterostructures have the straddling band structure characteristic, accumulating electrons and holes into the same components under light irradiation.[12] For type-III heterostructures, the bandgap of one monolayer is broken by the other component.[13] However, type-II heterostructures with staggered band structures are beneficial for efficient photocatalyst performance.[14] Based on the different carrier migration pathways, type-II heterostructures can be divided into conventional type-II and direct Z-schemes. The conventional type-II scheme has excellent photogenerated carrier utilization capacity, but diminished redox capacity.[15] Conversely, the direct Z-scheme can improve the redox capacity and have excellent light absorption performance that can drive HERs in the higher conduction band minimum (CBM) of two components and the OERs in the lower valence band maximum (VBM).[16] Thus, constructing direct Z-scheme heterostructures is a smart choice to obtain efficient photocatalyst materials. For example, $ZnIn_2S_4$/$MoSe_2$ [17] with a direct Z-scheme fabricated through an experiment exhibits an optimized apparent quantum yield and a high hydrogen-production rate. In_2O_3/$ZnInSe_4$,[18] TiO_2/$ZnIn_2S_4$,[19] and $Cd_{0.5}Zn_{0.5}S$/$BiVO_4F$ [20] heterostructures display a more excellent photocatalyst performance than the monolayers composing them. The theoretically proposed $PtTe_2$/Sb_2S_3,[21] C_7N_6/Sc_2CCl_2,[22] and C_7N_6/GaSnPS [23] with direct Z-schemes further demonstrate

[a]School of Physics and Optoelectronic Engineering, Ludong University, Yantai 264025, China. E-mail: ycl@ldu.edu.cn
[b]Xinjiang Astronomical Observatory, Chinese Academy of Sciences, Urumqi 830011, China
[c]Key Laboratory of Radio Astronomy, Chinese Academy of Sciences, Urumqi 830011, China

† Electronic supplementary information (ESI) available. See DOI: https://doi.org/10.1039/d3ta06755f

outstanding light absorption and carrier separation abilities. Dual Z-scheme heterostructures constructed from three monolayers with a narrow bandgap can achieve a wide light absorption range, which is one of the crucial factors for enhancing the photocatalyst performance. Generally, the dual Z-scheme of trilayer heterostructures is divided into arrow-up,[24] arrow-down,[25] and cascade[26,27] according to the characteristics of band alignments. Considering that the HER and OER can occur in nonadjacent monolayers in dual Z-scheme heterostructures, the lifetime of photogenerated carriers in a trilayer heterostructure is prolonged, which is conducive to suppressing the recombination of carriers.[28,29] Meanwhile, the shape and size of different materials can be controlled, resulting in the large specific surface area and the high photocatalytic activity of a trilayer heterostructure. Carrier migration mechanisms with different types of band alignments have been suggested in some experimental reports, such as the V_2O_5/CdS/CoS_2,[30] BiSi/Bi_2WO_6/g-C_3N_4,[31] and AgI/g-C_3N_4/Bi_2WO_6 [32] trilayer heterostructures. However, they have not been confirmed theoretically. Therefore, intensive theoretical studies of the carrier migration mechanism of trilayer heterostructures are urgently needed.

Two-dimensional (2D) transition metal dichalcogenide $HfSe_2$ and $ZrSe_2$ monolayers reportedly have attractive electronic and optical properties.[33–35] For example, the $HfSe_2$/$ZrSe_2$ heterostructure has been reported to have a type-I band alignment, and the potential of CBMs cannot straddle the hydrogen reduction potential (−4.44 eV).[36] We have first constructed sandwich heterostructures by stacking[37,38] and doping[11,39] methods, which have turned out to be effective measures to regulate band alignment. However, the working CBM of $HfSe_2$/$ZrSe_2$/$HfSe_2$ and $ZrSe_2$/$HfSe_2$/$ZrSe_2$ configurations cannot match the HER condition. The band alignment of the $HfSe_2$/$ZrSe_2$ heterostructure can be changed to type II by doping Te atoms into the $HfSe_2$ monolayer. We have also considered two different configurations of the HfSeTe/$ZrSe_2$ heterostructures. However, we have found that only the HfSeTe/$ZrSe_2$-I heterostructure can straddle the potentials of the HER and OER, whereas the overpotential for the HER is only 0.03 eV even though the η'_{STH} is 22.08%. Subsequently, four sandwich configurations constructed from the HfSeTe and $ZrSe_2$ monolayers have also been explored, whereas their band alignment types are arrow-up or arrow-down. The CBMs and VBMs cannot fully match the potential conditions of HERs or OERs. In the present study, we constructed eight different configurations of 2D trilayer heterostructures by adding the Bi or $InAs_3$ monolayer on the bilayer HfSeTe/$ZrSe_2$ heterostructure. As expected, the Bi/HfSeTe/$ZrSe_2$-I, Bi/HfSeTe/$ZrSe_2$-II, and $InAs_3$/HfSeTe/$ZrSe_2$-I configurations had cascade band alignment, by which we constructed cascade dual Z-schemes. The obtained schemes also satisfied the potential requirements of the HER and OER. The η'_{STH}'s on Bi/HfSeTe/$ZrSe_2$-I, Bi/HfSeTe/$ZrSe_2$-II, and $InAs_3$/HfSeTe/$ZrSe_2$-I can reach 40.52%, 39.47%, and 41.04%, respectively. The η'_{STH} was further boosted to 41.53%, 41.12%, and 43.57% under 1%, 1%, and −2% biaxial strain, respectively. Additionally, the protection of the redox ability in cascade dual Z-scheme heterostructures is demonstrated using the carrier transfer speeds through non-adiabatic molecular dynamics (NAMD)[40] simulations. The Gibbs free energy changes (ΔG) indicated that HERs and OERs were thermodynamically feasible. Remarkably, the HER and OER with Bi/HfSeTe/$ZrSe_2$-II can proceed spontaneously in a neutral environment because the potential energies of the photogenerated electrons and holes were larger than the ΔG's in the HER and OER, respectively. Therefore, these trilayer heterostructures had competitive potential to achieve high STH efficiency through the cascade dual Z-scheme.

2. Computational methods

The HfSeTe monolayer was constructed by replacing all Se atoms on the same side of the $HfSe_2$ monolayer with Te atoms. The present HfSeTe, $ZrSe_2$, and $InAs_3$ monolayers were with the symmetry of the *p*3*m*1 space group, and the Bi monolayer belonged to the *p*6*m*2 space group, as shown in Fig. S1.† Trilayer heterostructures were constructed by adding the third monolayer to the top or bottom of $HfSe_2$/$ZrSe_2$ or HfSeTe/$ZrSe_2$ bilayer heterostructures. For all heterostructures containing the HfSeTe monolayer, we also considered two different configurations (HfSeTe monolayer rotating 180° along the *y* direction), which were represented by HfSeTe/$ZrSe_2$-I, HfSeTe/$ZrSe_2$-II, $ZrSe_2$/HfSeTe/$ZrSe_2$-I, HfSeTe/$ZrSe_2$/HfSeTe-II, HfSeTe/$ZrSe_2$/HfSeTe-III, $ZrSe_2$/HfSeTe/$ZrSe_2$, Bi/HfSeTe/$ZrSe_2$-I, Bi/HfSeTe/$ZrSe_2$-II, HfSeTe/$ZrSe_2$/Bi-I, HfSeTe/$ZrSe_2$/Bi-II, $InAs_3$/HfSeTe/$ZrSe_2$-I, $InAs_3$/HfSeTe/$ZrSe_2$-II, HfSeTe/$ZrSe_2$/$InAs_3$-I, and HfSeTe/$ZrSe_2$/$InAs_3$-II. The interlayer distances (*d*) and formation energies (E_f) for 16 configurations are listed in Table S1.†

All calculations for the geometrical optimization and electronic and optical properties were realized in the Vienna *ab intitio* simulation package (VASP).[41] The projector augmented wave[42] pseudopotentials in combination with the generalized gradient approximation with Perdew–Burke–Ernzerhof[43] and Heyd–Scuseria–Ernzerhof (HSE06)[44] hybrid functionals were used. The dipole correction was added along the *z* direction in all calculations to correct the potential and force because of the asymmetric monolayers in the heterostructures. The cutoff energy was used at 550 eV for the plane wave. The density functional dispersion correction (DFT-D4)[45,46] was used to describe the van der Waals interactions. The energy and force convergence standards were selected as 10^{-6} eV and 0.01 eV $Å^{-1}$, respectively. Geometric structures were optimized and static calculations of electronic properties were performed using HSE06 with a 3 × 3 × 1 and 5 × 5 × 1 *k*-mesh, respectively. *Ab initio* molecular dynamics (AIMD) simulations for the screened structures lasting 10 ps at 300 K based on the Nose–Hoover thermostat and a canonical ensemble (NVT)[47,48] were conducted to confirm the thermodynamic stability of the heterostructures. NAMD simulations combined with decoherence-induced surface hopping (DISH)[49] methods implemented in the Hefei-NAMD code[40] were used to study the migration pathway and lifetimes of the photogenerated carriers. For the DISH simulation, we selected 100 random initial configurations and sampled 2000 trajectories, expanding the simulation time to 10 ps.

The calculation methods and details for the η'_{STH}'s, optical absorption, carrier mobility, ΔG's in the HER and OER, and NAMD simulation are presented in the ESI.†

3. Results and discussion

3.1 Bilayer heterostructures composed of $HfSe_2$ and $ZrSe_2$ monolayers

$HfSe_2$ and $ZrSe_2$ monolayers were prepared in the experiment and showed excellent thermal and optical properties,[33,50] whereas the $HfSe_2/ZrSe_2$ heterostructure[36] was found to have a type-I band alignment. The CBM and VBM contributed by the $ZrSe_2$ monolayer did not match the overall water splitting conditions. To manipulate the photocatalyst performance, we constructed $HfSe_2/ZrSe_2/HfSe_2$ and $ZrSe_2/HfSe_2/ZrSe_2$ sandwich configurations, as shown in Fig. 1a and d. The negative formation energies (E_f's) of −35.74 and −37.82 meV Å^{-2} indicated that they were stable in energy. The band structures and projected density of states (PDOS) are presented in Fig. 1b and e. They showed that the band of the sandwich configurations changed into a dual type-I arrangement. The charge transfer between the adjacent monolayers was decided by the direction of the built-in electron field (E_{in})[51] through Bader charge analysis[52] and plane-integrated charge density difference ($\Delta\rho$). As shown in Fig. S1a,† the charge transfer of 0.0012 and 0.0016 $|e|$ occurs from the bottom and top $HfSe_2$ to the $ZrSe_2$ monolayer, together with the accumulated electrons on both sides of the $ZrSe_2$ monolayers, given by $\Delta\rho$s, indicating that the E_{in} directions between the two interfaces of the $HfSe_2/ZrSe_2/HfSe_2$ heterostructure were from the $HfSe_2$ to the $ZrSe_2$ monolayers. As shown in Fig. 1c, the photogenerated electrons in the CBM of $ZrSe_2$ transferred into the CBM of $HfSe_2$ monolayers, whereas the holes in the VBM of $HfSe_2$ transferred into the VBM of the $ZrSe_2$ monolayer. Therefore, the HER occurred in the CBMs of the two $HfSe_2$ monolayers, and the OER was driven by the middle $ZrSe_2$ monolayer.

For $ZrSe_2/HfSe_2/ZrSe_2$, Fig. S1b† demonstrates that 0.0015 and 0.0014$|e|$ transferred from the two $ZrSe_2$ monolayers into the $HfSe_2$ one. Combining the band alignment and E_{in} at the two interfaces, the photogenerated electrons in the CBMs of the two $ZrSe_2$ monolayers were found to spontaneously transfer into the CBM of the $HfSe_2$ monolayer, whereas the holes in the VBM of the $HfSe_2$ monolayer transferred into the VBMs of the two $ZrSe_2$ monolayers (Fig. 1f). Therefore, the electrons in the CBM of the $HfSe_2$ and the holes in the VBM of the $ZrSe_2$ monolayers proceeded to undergo the HER and OER, respectively.

The absolute band edges can be evaluated by the following equations:

$$E_{CBM}^{Abs} = E_{CBM}^{HSE06} - V_{vac} \quad (1)$$

$$E_{VBM}^{Abs} = E_{VBM}^{HSE06} - V_{vac} \quad (2)$$

where E_{CBM}^{HSE06}/ E_{CBM}^{HSE06} represent the energies of the CBM and VBM calculated by the HSE06 functional, respectively, and V_{vac} represents the values obtained from the electrostatic potential plots, as shown in Fig. S2 and S3.† Unfortunately, the E_{CBM}^{Abs}'s cannot match the HER condition, although the E_{VBM}^{Abs}'s of the $HfSe_2/ZrSe_2/HfSe_2$ and $ZrSe_2/HfSe_2/ZrSe_2$ configurations can satisfy the OER requirement.

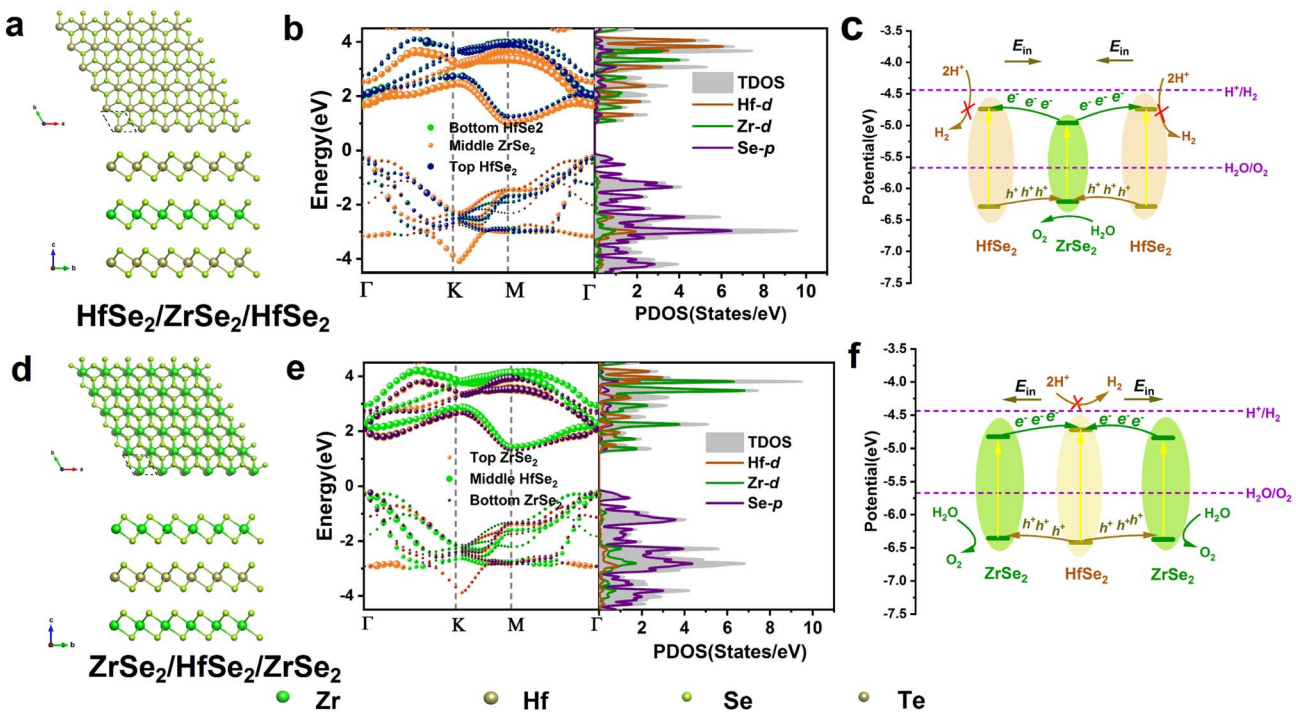

Fig. 1 The geometric structures, band alignments, projected density of states, and the schemes for HERs and OERs. (a)–(c) $HfSe_2/ZrSe_2/HfSe_2$, and (d)–(f) $ZrSe_2/HfSe_2/ZrSe_2$.

3.2 Bilayer HfSeTe/$ZrSe_2$ and trilayer HfSeTe/$ZrSe_2$/HfSeTe and $ZrSe_2$/HfSeTe/$ZrSe_2$ sandwich heterostructures

The electronic properties of monolayers and heterostructures can be significantly controlled by doped atoms.[39,53] Thus, the heterostructure comprising the Te-doped $HfSe_2$ monolayer, *i.e.*, HfSeTe, was explored. The geometric structure, band alignment, and PDOS of the HfSeTe monolayer are shown in Fig. S4a and b.† The present direct bandgap of 0.39 eV of the HfSeTe monolayer was close to the previous ones of 0.44 [54] and 0.47 eV,[55] confirming that the present theoretical level was reliable. The HfSeTe monolayer can also be synthesized by chemical vapor deposition or conventional flux methods experimentally, such as the fabrication of MoSSe [56] and MoSeTe.[57] Accordingly, we constructed bilayer and trilayer heterostructures by using the HfSeTe and $ZrSe_2$ monolayers. Nowadays, the MoSSe/MoS_2,[58] MoS_2/WSe_2,[59] and $ZrSe_2$/$MoSe_2$ [60] heterostructures are synthesized by mechanical exfoliation, chemical vapor deposition, and dry transfer methods, so the bilayer heterostructure of HfSeTe/$ZrSe_2$ may be synthesized in the same ways because of the similar structures. We considered two configurations of the HfSeTe/$ZrSe_2$ heterostructure, as shown in Fig. 2a and d. The negative E_f's of −21.65 and −19.48 meV Å^{-2} meant that the HfSeTe/$ZrSe_2$ heterostructures can be synthesized through an exothermic process. The insignificant deformation of the geometric structures in the AIMD simulations in Fig. S5a and b† indicated that they were thermodynamically stable. Staggered band alignments were observed for the HfSeTe/$ZrSe_2$-I and HfSeTe/$ZrSe_2$-II configurations, as shown in Fig. 2b and e. The E_{in} directions from HfSeTe to the $ZrSe_2$ monolayer in the heterostructures can propel the electrons transferring from the $ZrSe_2$ into the HfSeTe monolayer, as shown in Fig. S1c and d.† Therefore, the photogenerated electrons in the CBM of the $ZrSe_2$ monolayer recombined with the holes in the VBM@HfSeTe. As a result, direct Z-schemes formed with the HER proceeding on the CBM@HfSeTe and the OER on the VBM@$ZrSe_2$, respectively. However, as presented in Fig. 2c and f, the CBM of HfSeTe/$ZrSe_2$-II cannot satisfy the HER condition, whereas the HER overpotential of 0.03 eV for HfSeTe/$ZrSe_2$-I implied a weak reduction ability.

Furthermore, three sandwich configurations of HfSeTe/$ZrSe_2$/HfSeTe-I, HfSeTe/$ZrSe_2$/HfSeTe-II, and HfSeTe/$ZrSe_2$/HfSeTe-III were considered, as shown in Fig. 2g, j and m. The band alignments in Fig. 2h, k and n showed a staggered and arrow-down feature, whereas the directions of E_{in} between the adjacent monolayers were from the HfSeTe to the $ZrSe_2$ monolayers. As shown in Fig. 2i, l and o, all three configurations were suitable for constructing a dual Z-scheme with HERs proceeding on the HfSeTe monolayers and OERs on the middle $ZrSe_2$ monolayer. Unlike the single V_{vac}'s for HfSeTe/$ZrSe_2$/HfSeTe-I and HfSeTe/$ZrSe_2$/HfSeTe-III, the HfSeTe/$ZrSe_2$/HfSeTe-II had different vacuum energy levels on the two surfaces. Thus, we evaluated E_{CBM}^{Abs} and E_{VBM}^{Abs} with different V_{vac}'s according to eqn (1) and (2). Results demonstrated that only one of the two CBMs relative to the two HfSeTe monolayers can straddle the hydrogen reduction potential, although all VBMs of the three configurations can drive the OER. Consequently, these heterostructures were not considered in the following discussion because they were similar to the bilayer heterostructures discussed in the above sections.

The trilayer sandwich configuration $ZrSe_2$/HfSeTe/$ZrSe_2$ had a staggered arrow-up type band alignment, and the directions of E_{in} were also from the HfSeTe into the $ZrSe_2$ monolayer, as shown in Fig. 2q and S1h.† The photocatalytic dual Z-scheme with the HER on CBM@HfSeTe and the OER on both $ZrSe_2$ monolayers is shown in Fig. 2r. However, CBMs@HfSeTe in Table S1,† regardless of any one of the two V_{vac}'s, failed to match the HER condition of −4.44 eV. Therefore, these sandwich configurations cannot drive the HER. The sandwich configurations, which were relatively more easily prepared than the trilayer heterostructures with three different monolayers, conferred difficulty in achieving an efficient photocatalytic overall water-splitting performance, although the dual Z-scheme can be constructed for some of them.

3.3 Dual Z-scheme heterostructures comprising Bi/$InAs_3$, HfSeTe, and $ZrSe_2$ monolayers

Trilayer Bi/HfSeTe/$ZrSe_2$ and $InAs_3$/HfSeTe/$ZrSe_2$ heterostructures were constructed by adding the $InAs_3$ or Bi monolayer onto the bilayer HfSeTe/$ZrSe_2$ heterostructure, respectively. The synthesis procedure similar to the bilayer heterostructures can also be used to prepare trilayer heterostructures, as demonstrated by the preparations of the $BiFeO_3$/g-C_3N_4/WO_3,[24] Ag_3PO_4/AgBr/g-C_3N_4,[28] and V_2O_5/CdS/CoS_2 heterostructures.[30] Thus, the present Bi/HfSeTe/$ZrSe_2$ and $InAs_3$/HfSeTe/$ZrSe_2$ heterostructures may be fabricated in a similar way. The $InAs_3$ and Bi monolayers optimized and calculated by HSE06 are shown in Fig. S4e–h.† The lattice constant and bandgap of 4.22 Å and 1.02 eV for the Bi monolayer approached the theoretical 4.24 Å and 1.16 eV obtained by Singh *et al.*,[61] whereas those for the $InAs_3$ monolayer were 7.85 Å and 1.19 eV, respectively. The CBMs of the two monolayers can match the HER condition, but the VBMs cannot satisfy the OER one, as demonstrated in Table S2.† Considering that the primary cells of the two monolayers substantially differed from the bilayer HfSeTe/$ZrSe_2$ heterostructures, we constructed trilayer heterostructures by using the 2×2 supercell of the HfSeTe/$ZrSe_2$ heterostructures and the $\sqrt{3} \times \sqrt{3}$ supercell of Bi or the primary cell of the $InAs_3$ monolayer. As a result, the lattice mismatch ratios of the Bi/HfSeTe/$ZrSe_2$ and $InAs_3$/HfSeTe/$ZrSe_2$ heterostructures were <1.5%.

Eight different configurations were considered and represented by Bi/HfSeTe/$ZrSe_2$-I, Bi/HfSeTe/$ZrSe_2$-II, HfSeTe/$ZrSe_2$/Bi-I, HfSeTe/$ZrSe_2$/Bi-II, $InAs_3$/HfSeTe/$ZrSe_2$-I, $InAs_3$/HfSeTe/$ZrSe_2$-II, HfSeTe/$ZrSe_2$/$InAs_3$-I, and HfSeTe/$ZrSe_2$/$InAs_3$-II. Their geometric structures, band structures, and carrier migration pathways are shown in Fig. S7 and S3.† The negative E_f's in Table S1† demonstrated that the heterostructures are stable in energy. The band alignments of HfSeTe/$ZrSe_2$/Bi-I, HfSeTe/$ZrSe_2$/Bi-II, and HfSeTe/$ZrSe_2$/$InAs_3$-I were arrow-down, whereas those of HfSeTe/$ZrSe_2$/$InAs_3$-II were arrow-up (Fig. S7b, e, k, n†). The $InAs_3$/HfSeTe/$ZrSe_2$-II band alignment was the type-I and type-II on the two interfaces, respectively (Fig. S7h†), thereby

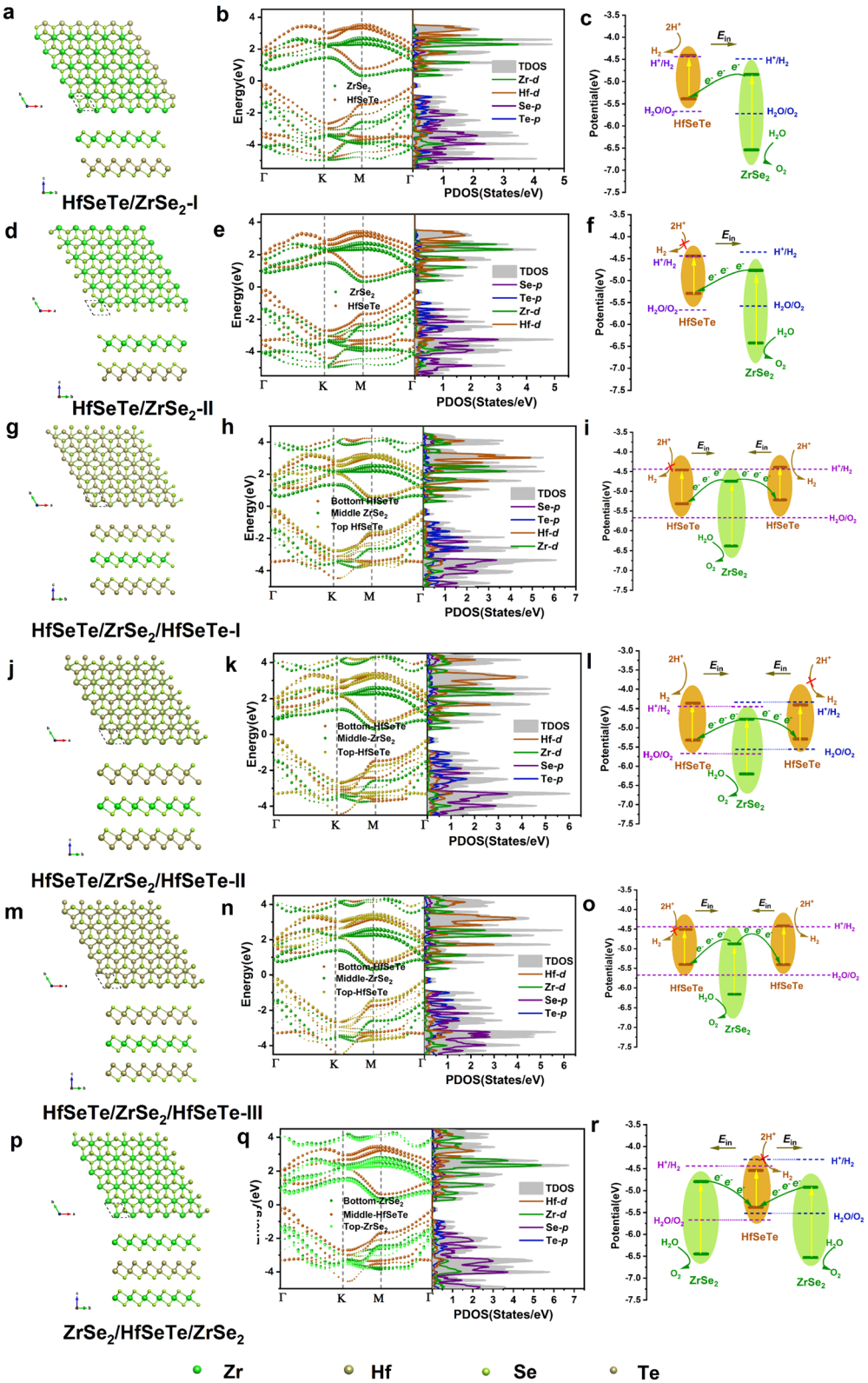

Fig. 2 The geometric structures, band alignments, project density of states, and the schemes for HERs and OERs. (a)–(c) HfSeTe/$ZrSe_2$-I, (d)–(f) HfSeTe/$ZrSe_2$-II, (g)–(i) HfSeTe/$ZrSe_2$/HfSeTe-I, (j)–(l) HfSeTe/$ZrSe_2$/HfSeTe-II, (m)–(o) HfSeTe/$ZrSe_2$/HfSeTe-III, and (p)–(r) $ZrSe_2$/HfSeTe/$ZrSe_2$.

losing the conditions necessary to form a dual Z-scheme. The E_{in} directions were from the bottom and top layers to the middle layer in the above five configurations, as shown in Fig. S1k, l, n, o and p.† The photocatalytic dual Z-schemes for HfSeTe/$ZrSe_2$/Bi-I, HfSeTe/$ZrSe_2$/Bi-II, and HfSeTe/$ZrSe_2$/$InAs_3$-I are shown in Fig. S7c, f and l.† Unfortunately, CBMs@HfSeTe cannot match the HER condition for the three trilayer heterostructures, although the VBMs in the middle layer satisfied the OER requirement. As shown in Fig. S7i,† CBM@$ZrSe_2$ in $InAs_3$/HfSeTe/$ZrSe_2$-II cannot meet the HER condition. As for the photocatalytic scheme of HfSeTe/$ZrSe_2$/$InAs_3$-II, the electrons in CBM@$ZrSe_2$ transferred into the CBMs of the $InAs_3$ and HfSeTe monolayers, and the holes in the VBM of the $InAs_3$ and HfSeTe transferred into VBMs@$ZrSe_2$, as presented in Fig. S7o.† Thus, the carrier migration in HfSeTe/$ZrSe_2$/$InAs_3$-II was a dual conventional type-II scheme rather than a dual Z-scheme. However, CBM@HfSeTe and VBM@$ZrSe_2$ cannot straddle the H^+/H_2 and H_2O/O_2 potentials, respectively. As a result, HfSeTe/$ZrSe_2$/Bi-I, HfSeTe/$ZrSe_2$/Bi-II, $InAs_3$/HfSeTe/$ZrSe_2$-II, HfSeTe/$ZrSe_2$/$InAs_3$-I, and HfSeTe/$ZrSe_2$/$InAs_3$-II cannot drive overall photocatalytic water splitting.

Notably, cascade band alignments were observed for Bi/HfSeTe/$ZrSe_2$-I, Bi/HfSeTe/$ZrSe_2$-II, and $InAs_3$/HfSeTe/$ZrSe_2$-I, as shown in Fig. 3b, e and h. Results of Bader charge analysis and $\Delta\rho$ in Fig. S1i, j and m† demonstrated that the E_{in} directions at the two interfaces of the heterostructures were arranged as bottom → middle → top monolayers. Accordingly, the electrons in CBM@$ZrSe_2$ recombined with the holes in VBM@HfSeTe, and the electrons in CBM@HfSeTe recombined with the holes in VBM@Bi or VBM@$InAs_3$. The outcome was the

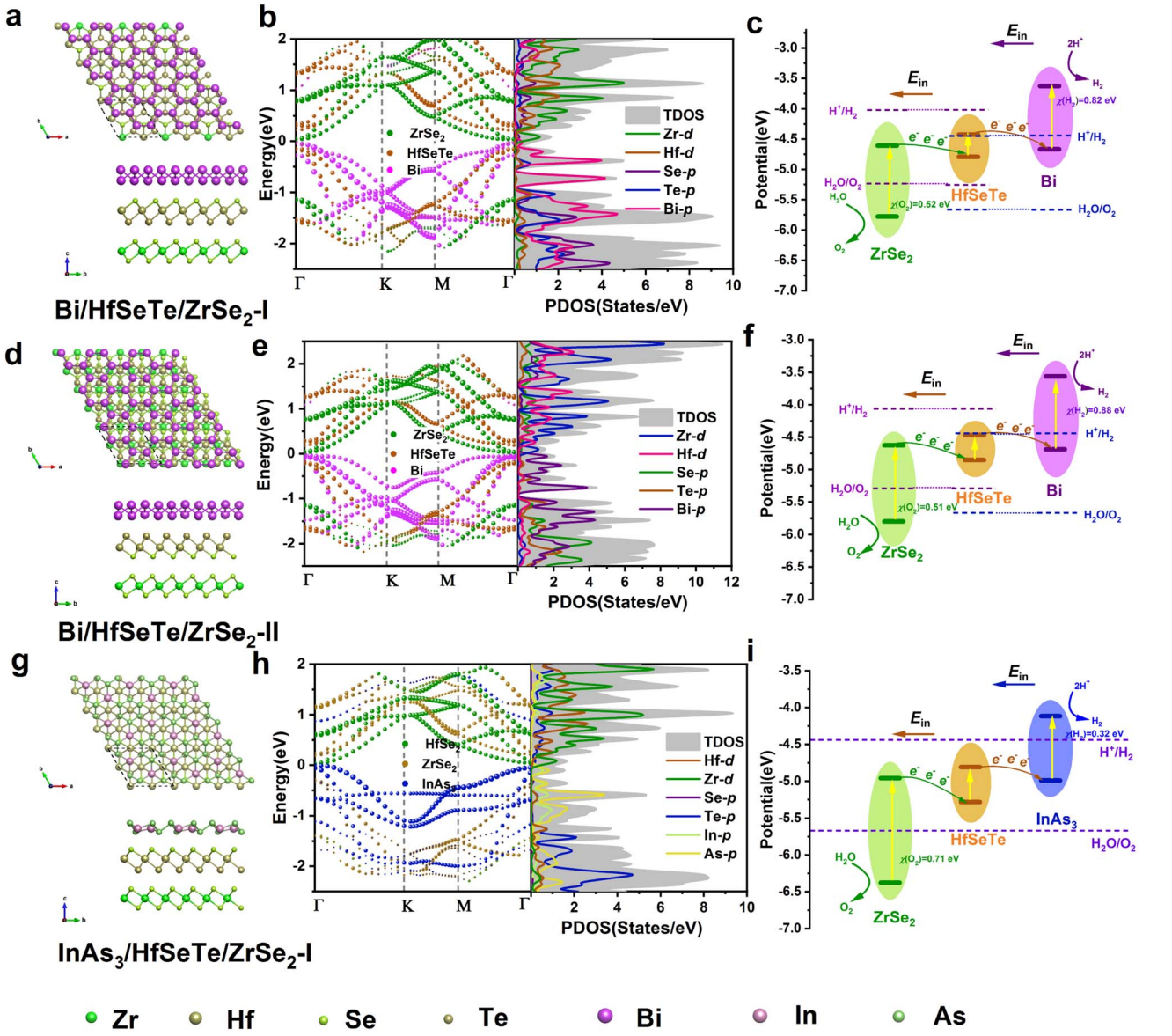

Fig. 3 The geometric structures, band alignments, project density of states, and the schemes for HERs and OERs. (a)–(c) Bi/HfSeTe/$ZrSe_2$-I, (d)–(f) Bi/HfSeTe/$ZrSe_2$-II, and (g)–(i) $InAs_3$/HfSeTe/$ZrSe_2$-I.

formation of a cascade dual Z-scheme, as shown in Fig. 3c, f and i. Therefore, the HER and OER were driven by CBM@Bi or CBM@$InAs_3$ and VBM@$ZrSe_2$, and all band edges of Bi/HfSeTe/$ZrSe_2$-I, Bi/HfSeTe/$ZrSe_2$-II, and $InAs_3$/HfSeTe/$ZrSe_2$-I can meet the conditions of the HER and OER, respectively. The working CBMs for HERs on Bi/HfSeTe/$ZrSe_2$-I and Bi/HfSeTe/$ZrSe_2$-II had larger overpotentials than those of $InAs_3$/HfSeTe/$ZrSe_2$-I, whereas their overpotentials for the OER were smaller than those of $InAs_3$/HfSeTe/$ZrSe_2$-II. As shown in Fig. S5c–e,† AIMD simulations at 300 K demonstrated that the three trilayer heterostructures were thermodynamically stable. Moreover, the stability of the considered heterostructures in the solution was explored by optimizing the geometric structures of the Bi/HfSeTe/$ZrSe_2$-I, Bi/HfSeTe/$ZrSe_2$-II, and $InAs_3$/HfSeTe/$ZrSe_2$-II trilayer heterostructures in the solution environments of water, formic acid, and acetone solvents using VASPsol,[62] respectively. As shown in Fig. S6,† the structures of the three configurations were obviously unchanged in the three neutral, acidic, and alkaline solutions, respectively. The solvation energy (ΔE_{sol}) of the three trilayer heterostructures, summarized in Table S3,† was defined by $\Delta E_{sol} = E_{sol} - E_{vac}$. In this equation, E_{sol} and E_{vac} represent the total energy of the heterostructures with and without solution, respectively. The negative ΔE_{sol}'s of the three trilayer heterostructures indicated that they were also stable in the solutions. Accordingly, we further explored the photocatalyst performance of Bi/HfSeTe/$ZrSe_2$-I, Bi/HfSeTe/$ZrSe_2$-II, and $InAs_3$/HfSeTe/$ZrSe_2$-I.

3.4 STH conversion efficiencies and effects of strain engineering

The STH conversion efficiencies η'_{STH}'s of the three trilayer heterostructures can be calculated by[63]

$$\eta'_{STH} = \frac{\Delta G \int_E^{\infty} \frac{P(\hbar\omega)}{\hbar\omega} d(\hbar\omega)}{\int_0^{\infty} P(\hbar\omega) d(\hbar\omega) + \Delta\varphi \int_{E_g}^{\infty} \frac{P(\hbar\omega)}{\hbar\omega} d(\hbar\omega)} \quad (3)$$

where $P(\hbar\omega)$ is the AM1.5 G solar-energy flux at the photo-energy $\hbar\omega$, E_g is the larger one of the bandgaps projected on the monolayers, and ΔG is the potential difference of 1.23 eV for water splitting. $\Delta\varphi$ is the electrostatic potential difference between the two outer surfaces, and E is the energy of photos that can actually be utilized for water splitting and evaluated by

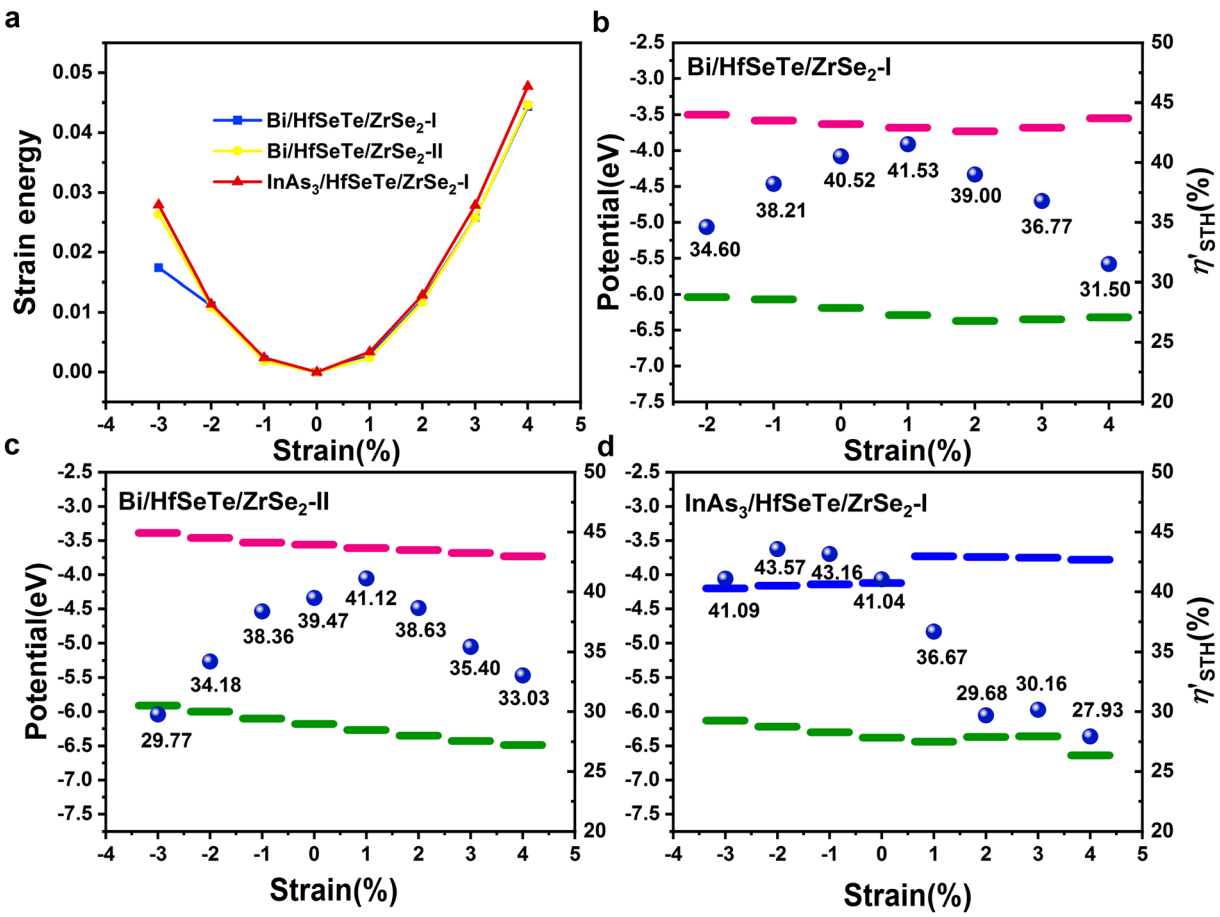

Fig. 4 The strain engineering for heterostructures. (a) The strain energies for Bi/HfSeTe/$ZrSe_2$-I, Bi/HfSeTe/$ZrSe_2$-II, and $InAs_3$/HfSeTe/$ZrSe_2$-I. (b)–(d) The potentials of band edges and STH conversion efficiency η'_{STH} of Bi/HfSeTe/$ZrSe_2$-I, Bi/HfSeTe/$ZrSe_2$-II, and $InAs_3$/HfSeTe/$ZrSe_2$-I under biaxial strains. The blue balls represent η'_{STH}.

$$E = \begin{cases} E_g, & (\chi(H_2) \geq 0.2,\ \chi(O_2) \geq 0.6) \\ E_g + 0.2 - \chi(H_2), & (\chi(H_2) < 0.2,\ \chi(O_2) \geq 0.6) \\ E_g + 0.6 - \chi(O_2), & (\chi(H_2) \geq 0.2, \chi(O_2) < 0.6) \\ E_g + 0.8 - \chi(H_2) - \chi(O_2), & (\chi(H_2) < 0.2,\ \chi(O_2) < 0.6) \end{cases} \quad (4)$$

The η'_{STH}'s for the three trilayer heterostructures Bi/HfSeTe/$ZrSe_2$-II, Bi/HfSeTe/$ZrSe_2$-II, and $InAs_3$/HfSeTe/$ZrSe_2$-I were 40.52%, 39.47%, and 41.04%, respectively. They were much higher than the 22.08% of the corresponding bilayer HfSeTe/$ZrSe_2$-I. According to eqn (S4)–(S7),† the smaller value of the maximum one of the bandgaps of monolayers and the larger overpotentials for the HER and OER were responsible for the high η'_{STH}. For the present trilayer heterostructures, the narrower bandgaps were the dominant factor causing the higher η'_{STH} than that of the bilayer one because the overpotentials of the working CBMs and VBMs of the trilayer heterostructures did not substantially increase. Notably, the η'_{STH}'s of Bi/HfSeTe/$ZrSe_2$-I, Bi/HfSeTe/$ZrSe_2$-II, and $InAs_3$/HfSeTe/$ZrSe_2$-II were much larger than those of ZrS_2/MoSSe (6.4%),[64] $HfSe_2$/InSe (25.24%),[15] and AlP_3/GaP_3 (16.89%).[65] Moreover, the η'_{STH} can also be compared with the experimental data if the AQE and experimental STH conversion efficiency (STH_{exp}) are available in the literature,[66] although the ideal quantum efficiency was used in eqn (3). For example, the GaN:Mg/InGaN:Mg nanowires[67] and Rh/Cr_2O_3/Co_3O_4-loaded InGaN/GaN nanowires[68] had STH_{exp}'s of 3.3% and 9% corresponding to the η'_{STH}'s of 7.5% and 17.7%, respectively. They were apparently lower than those of the present trilayer heterostructures.

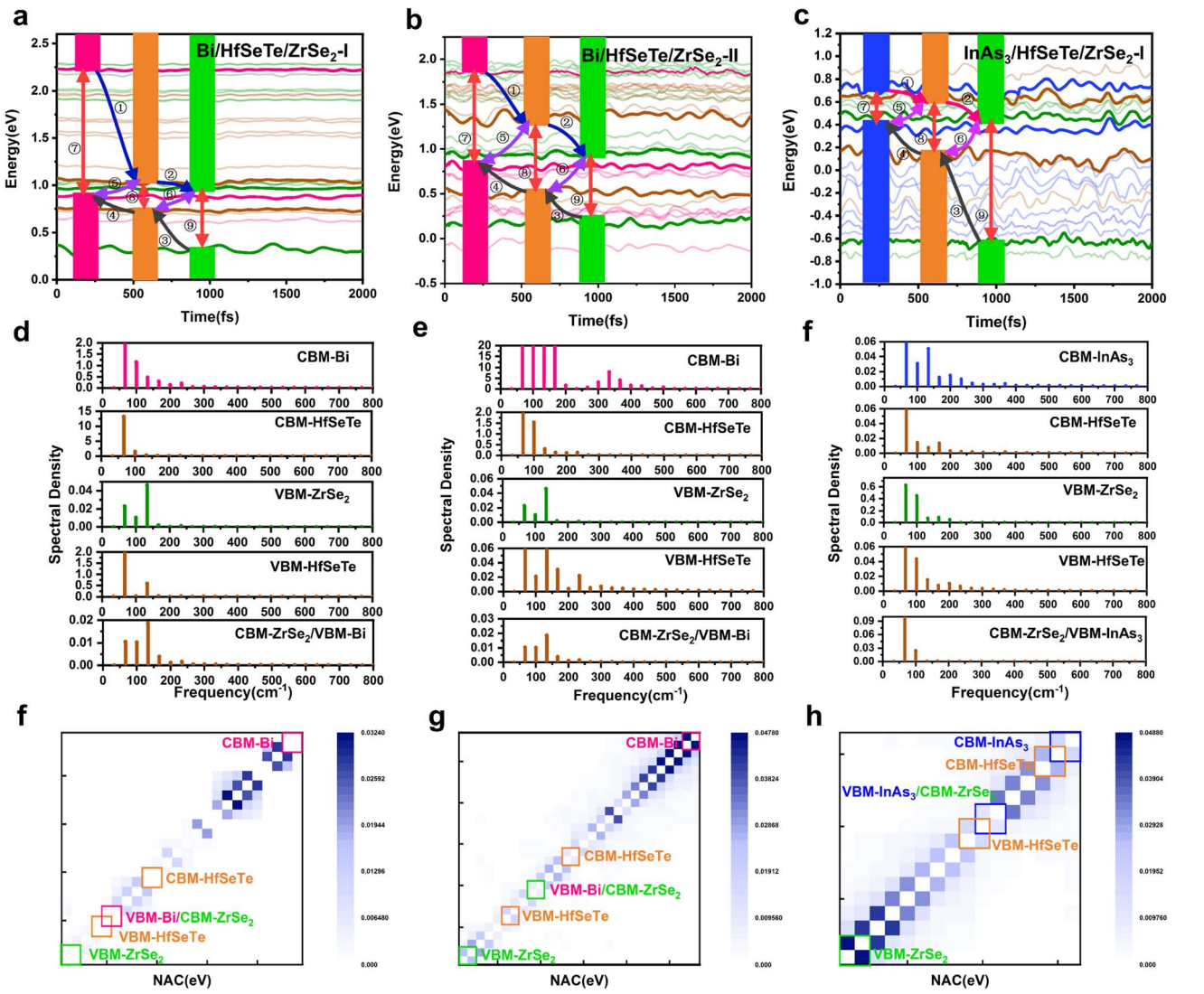

Fig. 5 The time-dependent evolution of the Kohn–Sham orbital, Fourier transforms of normalized ACF of the energy difference fluctuation between the initial and final states, and averaged values of NAC between different states for (a), (d) and (f) Bi/HfSeTe/$ZrSe_2$-I, (b), (e) and (g) Bi/HfSeTe/$ZrSe_2$-II, and (c), (f) and (h) $InAs_3$/HfSeTe/$ZrSe_2$-I. The purplish red, orange, and green lines in (a), (b), and (c) represent the states dominated by Bi, HfSeTe, and $ZrSe_2$ monolayers, respectively. The inset diagram shows nine photogenerated carrier dynamics pathways: the electron transfer (①②), the hole transfer (③④), the interlayer electron–hole recombination (⑤⑥), and the intralayer electron–hole recombination (⑦⑧⑨).

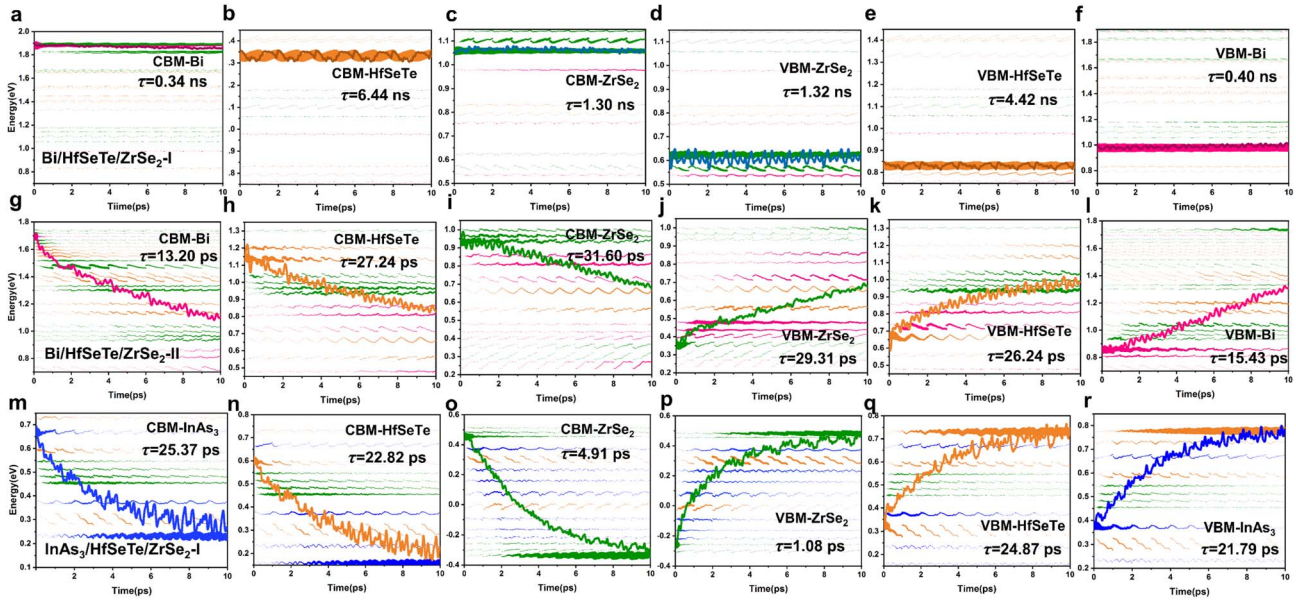

Fig. 6 The time-dependent evolution of the electron/hole spatial localization and distribution in each state in Bi/HfSeTe/$ZrSe_2$-I, Bi/HfSeTe/$ZrSe_2$-II, and $InAs_3$/HfSeTe/$ZrSe_2$-I. The purplish red, blue, orange, and green lines represent the energy states dominated by Bi, $InAs_3$, HfSeTe, and $ZrSe_2$ monolayers, respectively. The descent or ascent lines represent the evolution of the averaged energy of the carriers in the considered states. (a), (g) and (m) CBM@Bi/$InAs_3$, (b), (h) and (n) CBM@HfSeTe, (c), (i) and (o) CBM@$ZrSe_2$, (d), (j) and (p) VBM@$ZrSe_2$, (e), (k) and (q) VBM@HfSeTe, and (f), (l) and (r) VBM@Bi/$InAs_3$.

As shown in Fig. 4a, the Bi/HfSeTe/$ZrSe_2$-II and $InAs_3$/HfSeTe/$ZrSe_2$-I heterostructures can maintain stability within the range of −3% to +4% biaxial strain because their strain energy E_s showed a quadratic character. The deformations of Bi/HfSeTe/$ZrSe_2$-I cannot maintain elasticity under −3% compressed strain, and only the range of −2% to +4% strains was considered for this heterostructure. As shown in Fig. 4b–d and listed in Tables S4–S6,† the bandgaps and overpotentials changed under the strains. As a result, the η'_{STH} increased to 41.53% and 41.12% for Bi/HfSeTe/$ZrSe_2$-I and Bi/HfSeTe/$ZrSe_2$-II under 1% biaxial strain, respectively, whereas the other strains reduced the η'_{STH}'s because of the increased bandgap of the monolayers and the decreased overpotentials of HERs and OERs. For the same reasons, the η'_{STH} of $InAs_3$/HfSeTe/ZrSe-I was boosted under −3% to −1% compressed strains but decreased under the tensile strains. The maximum η'_{STH} of 43.57% for $InAs_3$/HfSeTe/ZrSe-I can be achieved under −2% compressed strains. Overall, most of the considered strains resulted in obviously decreased η'_{STH}, although smaller lifts were also observed for the light strains. Therefore, heavy strains, regardless of being compressive or tensile, should be avoided to maintain the high η'_{STH}'s of the present trilayer heterostructures.

3.5 Dynamics of photogenerated carriers for cascade dual Z-scheme heterostructures

To confirm the photocatalyst performance of Bi/HfSeTe/$ZrSe_2$-I, Bi/HfSeTe/$ZrSe_2$-II, and $InAs_3$/HfSeTe/$ZrSe_2$-I, we performed NAMD simulations by using the Hefei-NAMD[40] code (the details in ESI†) which has been used to analyze the carrier dynamics theoretically for the experimental observations of MoS_2/$MoSe_2$,[69,70] $ReSe_2$/MoS_2,[71,72] and MoS_2/WS_2.[73,74] As shown in Fig. 5a–c, nine different processes occurred in the trilayer heterostructure, including the electron transfer (①②), hole transfer (③④), interlayer e–h recombination (⑤⑥), and intralayer e–h recombination (⑦⑧⑨). Fig. 6 demonstrates that carriers tended to transfer into the adjacent states according to the evolution of the spatial distributions and the average energies of the carriers in each CBM and VBM of the three monolayers at 300 K for 10 ps based on the DISH.[49] Moreover, the carrier energy relaxation processes in the three trilayer heterostructures had different time scales, which can be understood through the nonadiabatic coupling (NAC) elements between different states.[75,76] In general, a large NAC corresponds to a higher hopping probability. According to eqn (S9),† a larger electron–phonon (e–p) coupling, a smaller energy gap, and a faster velocity of nuclei lead to a larger NAC matrix element. As shown in Fig. 5d–f, the Fourier transforms of the normalized autocorrelation function (ACF) for the fluctuations of the energy difference between the initial and final states were calculated and used to estimate the contribution of e–p coupling and nuclear velocity.[70] The low frequency and weak intensity peaks in the Fourier energy spectrum dominated the slow dephasing process,[77,78] and the long pure-dephasing time was also beneficial for ultrafast carrier transfer. As shown in Fig. S8 and S9,† the low-frequency modes were similar among the six processes in Bi/HfSeTe/$ZrSe_2$-I and Bi/HfSeTe/$ZrSe_2$-II. The peaks at 66 and 103 cm^{-1} correspond to the out-of-plane vibrations of the Hf–Se and Hf–Te bonds; the peaks at 140 and 202 cm^{-1} correspond to the out-of-plane vibration of Se, Te, Hf, and Zr atoms; and the side peaks near 262 cm^{-1} correspond to the vibration of Se and Zr atoms in the $ZrSe_2$ monolayer. This finding demonstrated their approximately equal nuclear velocities. As shown

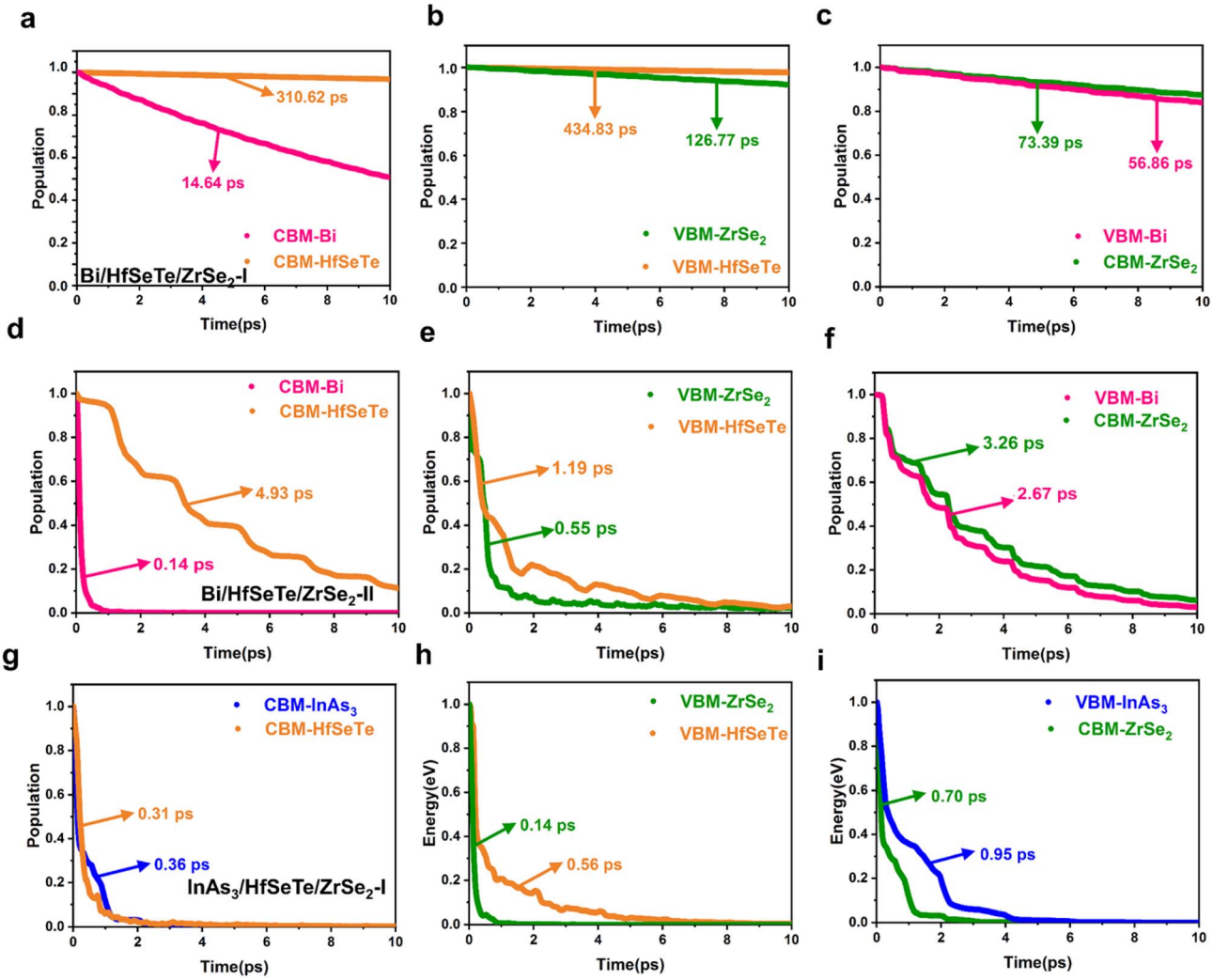

Fig. 7 The carrier transfer dynamics in Bi/HfSeTe/$ZrSe_2$-I, Bi/HfSeTe/$ZrSe_2$-II, and $InAs_3$/HfSeTe/$ZrSe_2$-I. (a), (d) and (g) CBM@Bi/$InAs_3$ and CBM@HfSeTe, (b), (e) and (h) VBM@$ZrSe_2$ and VBM@HfSeTe, and (c), (f) and (i) CBM@$ZrSe_2$ and VBM@Bi/$InAs_3$.

in Fig. S10,† all low-frequency vibration modes observed for the six processes in $InAs_3$/HfSeTe/$ZrSe_2$-I were contributed by the out-of-plane vibrations of all bonds, which increased the e–p coupling, causing fast carrier transfer.

As presented in Fig. 5f–h and listed in Tables S7–S9,† the strong NAC originating from the narrow bandgaps between the adjacent states accelerated the carrier transfer into the involved states. A few peaks existed in the spectral density of the six states of Bi/HfSeTe/$ZrSe_2$-I due to the gentle fluctuations of Kohn–Sham orbitals, demonstrating that the slight vibration of atoms contributed minimally to the NAC, as shown in Fig. 5f. Therefore, all energy relaxation processes in Bi/HfSeTe/$ZrSe_2$-I were slow, and the time scale difference in the six energy relaxation processes was nearly 10 times, which was averse to the transfer of carriers in the heterostructure and promoted the photocatalytic process, as shown in Fig. 6a–f. The numerous strong peaks, as well as the small bandgaps between CBM@Bi and the adjacent state in the Bi/HfSeTe/$ZrSe_2$-II, further led to the strongest NAC (47.17 meV) in the six energy states, as shown in Fig. 5g. Hence, the electron relaxation in the highest CBM was the quickest one among the six processes of Bi/HfSeTe/$ZrSe_2$-II, as shown in Fig. 6g–l. Similarly, the NAC between VBM@$ZrSe_2$ and the adjacent states was the strongest one (48.63 meV), as shown in Fig. 5h, so entire hole relaxation on this energy level was the quickest one among the six processes of $InAs_3$/HfSeTe/$ZrSe_2$-I, as shown in Fig. 6m–r. Moreover, all energy relaxation processes in Bi/HfSeTe/$ZrSe_2$-II were in the same time scale, which benefited the carrier cycling and were utilized in the photocatalysis.

The carrier population evolution relative to time in Fig. 7 demonstrated a characteristic of exponential function among the six transfer processes of the interlayer carriers. As in a previous analysis method,[69,79] we fit the time population evolutions with the function $f(t) = \exp(-t/\tau)$ to understand the evolution tendency. The τ corresponding to the carrier population of $1/e$ was defined as the carrier lifetime because the transfer process corresponding to this carrier population of an electronic state was considered irreversible and over. Generally, the slow carrier transfer in CBM@Bi/CBM@$InAs_3$ and VBM@$ZrSe_2$ was beneficial for the carriers to participate in the

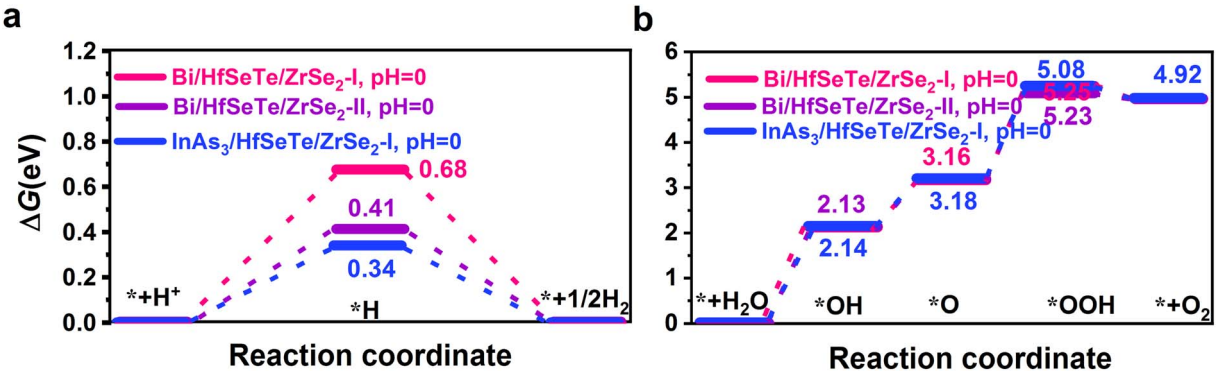

Fig. 8 The Gibbs free energy changes for (a) HERs and (b) OERs at pH = 0 of Bi/HfSeTe/$ZrSe_2$-I, Bi/HfSeTe/$ZrSe_2$-II, and $InAs_3$/HfSeTe/$ZrSe_2$-I, respectively.

redox reaction of the Z-schemes. As shown in Fig. 7, the longest carrier lifetimes of 14.64 and 126.77 ps were attributed to Bi/HfSeTe/$ZrSe_2$-I among the three heterostructures, indicating that the redox abilities of the two energy levels can be effectively protected. The Z-schemes with Bi/HfSeTe/$ZrSe_2$-II and $InAs_3$/HfSeTe/$ZrSe_2$-I were more efficient than that with Bi/HfSeTe/$ZrSe_2$-I owing to the quick carrier transfer migrations during the interlayer e–h recombination processes in CBM@HfSeTe, VBM@HfSeTe, CBM@$ZrSe_2$, and VBM@Bi/$InAs_3$ in the former two heterostructures. When the carrier migrations and recombination were involved, $InAs_3$/HfSeTe/$ZrSe_2$-I was superior to the others.

3.6 Gibbs free energies of the HER and OER

According to the Sabatier principle,[80] the closer the Gibbs free energy ΔG is to zero, the easier the reaction proceeds. As shown in Table S10,† the absorbed energy of the H atom on every unequal position demonstrated that the H atom preferred to adsorb onto the Bi_1 atom in Bi/HfSeTe/$ZrSe_2$-I and Bi/HfSeTe/$ZrSe_2$-II and on the In atom in $InAs_3$/HfSeTe/$ZrSe_2$-I. The adsorption sites with the lowest energy were selected to calculate the ΔGs for the HER and OER. The results are presented in Fig. S11.† The potential of the photogenerated electrons (U_e) for the HER was measured from the CBM to the H^+/H_2 potential, whereas that of the photogenerated holes (U_h) for the OER was determined by the difference between the VBM and the potential of H^+/H_2.[81,82] When the ΔG_{H^*}'s were less than eU_es, the HER proceeded spontaneously. Similarly, the OER spontaneously proceeded when all ΔG's of the intermediates in the OER (ΔG_{OER}'s) were less than the eU_h's. Considering that pH can impact the redox potentials of overall water splitting,[83] we calculated the ΔG's for the HER and OER with pH 0–14 according to the method described in the ESI.†

As shown in Fig. 8, the eU_e's with Bi/HfSeTe/$ZrSe_2$-I, Bi/HfSeTe/$ZrSe_2$-II, and $InAs_3$/HfSeTe/$ZrSe_2$-I were 0.81, 0.88, and 0.32 eV, respectively. The HERs at pH 0 on Bi/HfSeTe/$ZrSe_2$-I and Bi/HfSeTe/$ZrSe_2$-II can spontaneously proceed because the ΔG_{*H}'s of 0.68 and 0.41 eV were smaller than the corresponding eU_e's. However, the ΔG_{*H} of 0.34 eV with $InAs_3$/HfSeTe/$ZrSe_2$-I was 0.02 eV larger than the eU_e, indicating that the HER cannot spontaneously proceed. pH can affect the redox potentials for the HER and OER. As shown in Fig. S12,† the HERs on Bi/HfSeTe/$ZrSe_2$-I and Bi/HfSeTe/$ZrSe_2$-II spontaneously proceeded within the pH ranges of 0.0–2.37 and 0.0–7.97, respectively, although the HER on $InAs_3$/HfSeTe/$ZrSe_2$-I failed in all pH values. However, the ΔG_{*H}'s with Bi/HfSeTe/$ZrSe_2$-I were smaller than the reported values that have been experimentally determined on some materials (*e.g.*, 1.5 eV for Mo_2CO_2 [84]) for HERs, indicating that all of them were feasible if additional energy was provided. During the calculations of the Gibbs free energies of (ΔG_{max}'s), the reactions with the *OH intermediates were the rate-limiting steps for all considered OERs. The OERs with the three heterostructures had 2.13, 2.14, and 2.13 eV of ΔG_{max}'s, and spontaneously proceed within the pH ranges of 6.44–14, 6.78–14, and 3.22–14, as shown in Fig. S12.† If the HER and OER were involved, only Bi/HfSeTe/$ZrSe_2$-II can drive them to proceed spontaneously within pH 6.78–7.97.

4. Conclusions

We constructed cascade dual Z-schemes with very high STH efficiency by using the trilayer Bi/HfSeTe/$ZrSe_2$-I, Bi/HfSeTe/$ZrSe_2$-II, and $InAs_3$/HfSeTe/$ZrSe_2$-I heterostructures after examining eight trilayer heterostructures. We found that the bilayer or trilayer heterostructures comprising $HfSe_2$ and $ZrSe_2$ monolayers were type-I or dual type-I band alignments and cannot drive the HERs. Meanwhile, the HfSeTe/$ZrSe_2$-I heterostructure met the overall water splitting requirements but had low overpotentials for the HER. For the four sandwich configurations formed with the HfSeTe and $ZrSe_2$ monolayers, the CBMs and VBMs cannot simultaneously match the potential conditions of the HER and OER. The cascade dual Z-schemes with η'_{STH}'s of 40.52%, 39.47%, and 41.04% were constructed for Bi/HfSeTe/$ZrSe_2$-I, Bi/HfSeTe/$ZrSe_2$-II, and $InAs_3$/HfSeTe/$ZrSe_2$-I after examining eight configurations obtained by adding the Bi or $InAs_3$ monolayer into the bilayer HfSeTe/$ZrSe_2$ heterostructures. Results of NAMD simulations demonstrated that the redox abilities of the three cascade dual Z-scheme heterostructures, especially for Bi/HfSeTe/$ZrSe_2$-I, were protected because of the slow carrier migrations in CBM@Bi($InAs_3$) and VBM@$ZrSe_2$. The ΔG_{*H}'s and ΔG_{OER}'s demonstrated the thermodynamic feasibility of the HERs and OERs driven by the three trilayer

heterostructures. Remarkably, Bi/HfSeTe/$ZrSe_2$-II can drive the HER and OER to proceed spontaneously at pH 6.78–7.97. Therefore, Bi/HfSeTe/$ZrSe_2$-II was a candidate for developing an efficient photocatalyst for hydrogen production from overall water splitting. The cascade dual Z-scheme was a promising mechanism to achieve high STH efficiency and worth extending to develop more photocatalysts.

Author contributions

X. Q. Wan: data curation, investigation, writing-original draft preparation. C. L. Yang: conceptualization, methodology, supervision, writing – reviewing and editing. X. H. Li: methodology. Y. L. Liu: visualization. W. K. Zhao: software.

Conflicts of interest

The authors declare no competing financial interest.

Acknowledgements

This work is supported by the National Natural Science Foundation of China (Grant No. 12374232). C. L. Yang acknowledges the Xinjiang Tianchi Talent Program (2023).

References

1 T. Hisatomi and K. Domen, Reaction systems for solar hydrogen production *via* water splitting with particulate semiconductor photocatalysts, *Nat. Catal.*, 2019, **2**, 387–399.
2 J. Liu, Y. Liu, N. Liu, Y. Han, X. Zhang, H. Huang and Z. Kang, Metal-free efficient photocatalyst for stable visible water splitting *via* a two-electron pathway, *Science*, 2015, **347**, 970–974.
3 J. Kou, C. Lu, J. Wang, Y. Chen, Z. Xu and R. S. Varma, Selectivity enhancement in heterogeneous photocatalytic transformations, *Chem. Rev.*, 2017, **117**, 1445–1514.
4 X. X. Li, J. Zhao and J. L. Yang, Semi-hydrogenated BN sheet: a promising visible-light-driven photocatalyst for water splitting, *Sci. Rep.*, 2013, **3**, 1858.
5 Y. Ji, M. Yang, H. Dong, T. Hou, L. Wang and Y. Li, Two-dimensional germanium monochalcogenide photocatalyst for water splitting under ultraviolet, visible to near-infrared light, *Nanoscale*, 2017, **9**, 8608–8615.
6 V. Kiran, D. Mukherjee, R. N. Jenjeti and S. Sampath, Active guests in the MoS_2/$MoSe_2$ host lattice: efficient hydrogen evolution using few-layer alloys of $MoS_{2(1-x)}Se_{2x}$, *Nanoscale*, 2014, **6**, 12856–12863.
7 Y. Fan, X. Ma, J. Wang, X. Song, A. Wang, H. Liu and M. Zhao, Highly-efficient overall water splitting in 2D Janus group-III chalcogenide multilayers: the roles of intrinsic electric filed and vacancy defects, *Chin. Sci. Bull.*, 2020, **65**, 27–34.
8 X. Liu, P. Cheng, X. Zhang, T. Shen, J. Liu, *et al.*, Enhanced solar-to-hydrogen efficiency for photocatalytic water splitting based on a polarized heterostructure: the role of intrinsic dipoles in heterostructures, *J. Mater. Chem. A*, 2021, **9**, 14515–14523.
9 T. Zhao, J. Chen, X. Wang, M. Yao, *et al.*, Ab initio insights into electronic structures, optical and photocatalytic properties of Janus WXY (X/Y = O, S, Se, and Te), *Appl. Surf. Sci.*, 2021, **545**, 148968.
10 Y. Fan, X. Song, S. Qi, X. Ma and M. Zhao, Li-III–VI bilayers for efficient photocatalytic overall water splitting: the role of the intrinsic electric field, *J. Mater. Chem. A*, 2019, **7**, 26123–26130.
11 Y. Fan, S. Qi, W. Li and M. Zhao, Direct Z-scheme photocatalytic CO_2 conversion to solar fuels in a two-dimensional C_2N/aza-CMP heterostructure, *Appl. Surf. Sci.*, 2021, **541**, 148630.
12 V. O. Özçelik, J. G. Azadani, C. Yang, S. J. Koester and T. Low, Band alignment of two-dimensional semiconductors for designing heterostructures with momentum space matching, *Phys. Rev. B*, 2016, **94**, 035125.
13 C. Lei, Y. Ma, X. Xu, T. Zhang, B. Huang, *et al.*, Broken-gap type-III and alignment in WTe_2/HfS_2 van der Waals heterostructure, *J. Phys. Chem. C*, 2019, **123**, 23089–23095.
14 Q. K. Yin, C. L. Yang, M. S. Wang and X. G. Ma, Two-dimensional heterostructures of AuSe/SnS for the photocatalytic hydrogen evolution reaction with a Z-scheme, *J. Mater. Chem. C*, 2021, **9**, 12231–12238.
15 R. Sun, C. L. Yang, M. S. Wang and X. G. Ma, High solar-to-hydrogen efficiency photocatalytic hydrogen evolution reaction with the $HfSe_2$/InSe heterostructure, *J. Power Sources*, 2022, **547**, 232008.
16 Q. K. Yin, C. L. Yang, M. S. Wang and X. G. Ma, Two-dimensional AuSe/SnSe heterostructure for solar photocatalytic hydrogen evolution reaction with Z-scheme, *Sol. Energy Mater. Sol. Cells*, 2022, **247**, 111940.
17 X. Wang, X. Wang, J. Huang, S. Li, A. Meng and Z. Li, Interfacial chemical bond and internal electric field modulated Z-scheme S_v-$ZnIn_2S_4$/$MoSe_2$ photocatalyst for efficient hydrogen evolution, *Nat. Commun.*, 2021, **12**, 4112.
18 Y. Chao, P. Zhou, N. Li, J. Lai, Y. Yang, Y. Zhang, *et al.*, Ultrathin visible-light-driven Mo Incorporating In_2O_3–$ZnIn_2Se_4$ Z-Scheme Nanosheet Photocatalysts, *Adv. Mater.*, 2019, **31**, 1807226.
19 G. Zuo, Y. Wang, W. L. Teo, Q. Xian and Y. Zhao, Direct Z-scheme TiO_2–$ZnIn_2S_4$ nanoflowers for cocatalyst-free photocatalytic water splitting, *Appl. Catal., B*, 2021, **291**, 120126.
20 C. Zeng, Y. Hu, T. Zhang, F. Dong, Y. Zhang, *et al.*, Core-Satellite structured Z-scheme catalyst $Cd_{0.5}Zn_{0.5}S$/$BiVO_4$ for highly efficient and stable photocatalytic water splitting, *J. Mater. Chem. A*, 2018, **6**, 16932–16942.
21 F. Wang, C. L. Yang, M. S. Wang and X. G. Ma, $PtTe_2$/Sb_2S_3 nanoscale heterostructures for the photocatalytic direct Z-scheme with high solar-to-hydrogen efficiency: a theoretical investigation, *ACS Appl. Nano Mater.*, 2023, **6**, 5591–5601.
22 J. Meng, J. Wang, J. Wang, Q. Li, *et al.*, C_7N_6/Sc_2CCl_2 Weak van der Waals heterostructure: A promising visible-lLight-driven Z-scheme water splitting photocatalyst with interface ultrafast carrier recombination, *J. Phys. Chem. Lett.*, 2022, **13**, 1473–1479.

23 J. Wang, X. Zhang, X. Song, Y. Fan, *et al.*, Insights into photoinduced carrier dynamics and overall water splitting of Z-scheme van der Waals heterostructures with intrinsic electric polarization, *J. Phys. Chem. Lett.*, 2023, **14**, 798–808.
24 S. Ali, M. Humayun, W. Pi, Y. Yuan and M. Wang, Fabrication of $BiFeO_3$-g-C_3N_4-WO_3 Z-scheme heterojunction as highly efficient visible-light photocatalyst for water reduction and 2,4-chlorophenol degradation: insight mechanism, *J. Hazard Mater.*, 2021, **397**, 22708.
25 X. Wang, G. Hai, B. Li, Q. Luan and W. Dong, *et, al.*, Construction of dual-Z-scheme WS_2–$WO_3 \cdot H_2O$/g-C_3N_4 catalyst for photocatalytic H_2 evolution under visible light, *Chem. Eng. J.*, 2021, **426**, 130822.
26 X. Li, H. Jiang, C. Ma, Z. Zhu, X. Song, H. Wang, *et al.*, Local surface plasma resonance effect enhanced Z-scheme ZnO/Au/g-C_3N_4 film photocatalyst for reduction of CO_2 to CO, *Appl. Catal., B*, 2021, **283**, 119638.
27 J. Jia, Q. Zhang, K. Li, Y. Zhang, E. Liu and X. Li, Recent advances on g–C_3N_4–based Z-scheme photocatalysts: Structural design and photocatalytic applications, *Int. J. Hydrogen Energy*, 2023, **48**, 196e231.
28 H. Yu, D. Wang, B. Zhao, Y. Lu, X. Wang, S. Zhu, *et al.*, Enhanced photocatalytic degradation of tetracycline under visible light by using a ternary photocatalyst of Ag_3PO_4/AgBr/g-C_3N_4 with dual Z-scheme heterojunction, *Sep. Purif. Technol.*, 2021, **237**, 16365.
29 M. Wang, G. Tan, H. Ren, A. Xia and Y. Liu, Direct double Z-scheme g-C_3N_4/Zn_2SnO_4N/ZnO ternary heterojunction photocatalyst with enhanced visible photocatalytic activity, *Appl. Surf. Sci.*, 2019, **492**, 690–702.
30 S. Sun, H. Cheng, K. Cao, A. Song, C. Xu, J. Ba, *et al.*, Ultrafast charge separation in ternary V_2O_5/CdS/CoS_2 Z-scheme heterojunction enables efficient visible-light-driven hydrogen generation, *Energy Fuels*, 2022, **36**, 2034–2043.
31 R. Zhang and K. Zeng, A novel flower-like dual Z-scheme BiSi/Bi_2WO_6/g-C_3N_4 photocatalyst has excellent photocatalytic activity for the degradation of organic pollutants under visible light, *Diamond Relat. Mater.*, 2021, **115**, 108343.
32 W. Xue, D. Huang, J. Li, G. Zeng, R. Deng, Y. Yang, *et al.*, Assembly of AgI nanoparticles and ultrathin g-C_3N_4 nanosheets codecorated Bi_2WO_6 direct dual Z-scheme photocatalyst: an efficient, sustainable and heterogeneous catalyst with enhanced photocatalytic performance, *Chem. Eng. J.*, 2019, **373**, 1144–1157.
33 K. E. Aretouli, P. Tsipas, D. Tsoutsou, *et al.*, Two-dimensional semiconductor $HfSe_2$ and $MoSe_2$/$HfSe_2$ van der Waals heterostructures by molecular beam epitaxy, *Appl. Phys. Lett.*, 2015, **106**, 143105.
34 P. Tsipas, D. Tsoutsou, J. Marquez-Velasco, *et al.*, Epitaxial $ZrSe_2$/$MoSe_2$ semiconductor van der Waals heterostructures on wide band gap AlN substrates, *Microelectron. Eng.*, 2015, **147**, 269–272.
35 M. J. Mleczko, C. Zhang, H. R. Lee and H. H. Kuo, *et, al.*, $HfSe_2$ and $ZrSe_2$: two-dimensional semiconductors with native high-κ oxides, *Sci. Adv.*, 2017, **3**, e1700481.
36 X. Q. Wan, C. L. Yang, M. S. Wang and X. G. Ma, Efficient photocatalytic hydrogen evolution and CO_2 reduction by $HfSe_2$/$GaAs_3$ and $ZrSe_2$/$GaAs_3$ heterostructures with direct Z-schemes, *Phys. Chem. Chem. Phys.*, 2023, **25**, 8861–8870.
37 R. Sivasamy, K. Paredes-Gil and J. V. Ramaclus, Sandwich-like GaN/$MoSe_2$/GaN heterostructure nanosheet: a first-principle study of the structure, electronic, optical, and thermodynamical properties, *Surf. Interfaces*, 2022, **34**, 102298.
38 D. S. Gavali, Y. Kawazoe and R. Thapa, First-principles identification of interface effect on Li storage capacity of C_3N/graphene multilayer heterostructure, *J. Colloid Interface Sci.*, 2022, **610**, 80–88.
39 X. Q. Wan, C. L. Yang, M. S. Wang and X. G. Ma, Boost solar-to-hydrogen efficiency by constructing heterostructures with the pristine and Se/Te-doped $AgInP_2S_6$ monolayers, *Appl. Surf. Sci.*, 2023, **614**, 156254.
40 Q. Zheng, W. Chu, C. Zhao and L. Zhang, *Ab initio* nonadiabatic molecular dynamics investigations on the excited carriers in condensed matter systems, *Wiley Interdiscip. Rev.: Comput. Mol. Sci.*, 2019, **9**, e1411.
41 G. Kresse and J. Furthmüller, Efficient iterative schemes for *ab initio* total-energy calculations using a plane-wave basis set, *Comput. Mater.*, 1996, **6**, 15–50.
42 P. E. Blöchl, Projector augmented-wave method, *Phys. Rev. B*, 1994, **50**, 17953–17979.
43 J. P. Perdew, K. Burke and M. Ernzerhof, Generalized gradient approximation made simple, *Phys. Rev. Lett.*, 1996, **77**, 3865.
44 S. Grimme, S. Ehrlich and L. Goerigk, Effect of the damping function in dispersion corrected density functional theory, *J. Comput. Chem.*, 2011, **32**, 1456–1465.
45 S. Grimme, S. Ehrlich and L. Goerigk, A consistent and accurate *ab initio* parametrization of density functional dispersion correction (DFT-D) for the 94 elements H-Pu, *J. Chem. Phys.*, 2010, **132**, 154104.
46 S. Nose, An extension of the canonical ensemble molecular dynamics method, *J. Phys. Chem. Lett.*, 1984, **81**, 511.
47 W. G. Hoover, Canonical dynamics: equilibrium phase-space distributions, *Phys. Rev. A*, 1985, **31**, 1695.
48 J. Heyd, G. E. Scuseria and M. Ernzerhof, Hybrid functionals based on a screened Coulomb potential, *J. Chem. Phys.*, 2003, **118**, 8207.
49 H. M. Jaeger, S. Fischer and O. V. Prezhdo, Decoherence-induced surface hopping, *J. Chem. Phys.*, 2012, **137**, 22a545.
50 Y. Tian, M. Zheng, Y. Cheng, *et al.*, Epitaxial growth of $ZrSe_2$ nanosheets on sapphire *via* chemical vapor deposition for optoelectronic application, *J. Mater. Chem. C*, 2021, **9**(39), 13954–13962.
51 K. Li, B. Peng and T. Peng, Recent advances in heterogeneous photocatalytic CO_2 conversion to solar fuels, *ACS Catal.*, 2016, **6**, 7485–7527.
52 R. F. W. Bader, Atoms in molecules: a quantum theory, *Adv. Quantum Chem.*, 1981, **14**, 63–124.
53 Y. Ji, M. Yang, H. Lin, T. Hou, L. Wang, Y. Li, *et al.*, Janus structures of transition metal dichalcogenides as the

heterojunction photocatalysts for water splitting, *J. Phys. Chem. C*, 2018, **122**, 3123–3129.
54 N. Jena, A. Rawat, R. Ahammed, M. K. Mohanta, *et al.*, Emergence of high piezoelectricity along with robust electron mobility in Janus structures in semiconducting Group IVB dichalcogenide monolayers, *J. Mater. Chem. A*, 2018, **6**, 24885–24898.
55 L. Wan, D. Chen, W. Zeng, J. Li and S. Xiao, Hazardous gas adsorption of Janus HfSeTe monolayer adjusted by surface vacancy defect: A DFT study, *Surf. Interfaces*, 2022, **34**, 102316.
56 A. Y. Lu, H. Zhu, J. Xiao, *et al.*, Janus monolayers of transition metal dichalcogenides, *Nat. Nanotechnol.*, 2017, **12**(8), 744–749.
57 P. Mudgal, H. Arora, J. Pati, *et al.*, Electrochemical investigation of MoSeTe as an anode for sodium-ion batteries, *Proc. Indian Natl. Sci. Acad.*, 2022, **88**(3), 430–438.
58 K. Zhang, Y. Guo, D. T. Larson, *et al.*, Spectroscopic signatures of interlayer coupling in Janus MoSSe/MoS_2 heterostructures, *ACS Nano*, 2021, **15**(9), 14394–14403.
59 K. Si, J. Ma, C. Lu, *et al.*, A two-dimensional MoS_2/WSe_2 van der Waals heterostructure for enhanced photoelectric performance, *Appl. Surf. Sci.*, 2020, **507**, 145082.
60 P. Tsipas, D. Tsoutsou, J. Marquez-Velasco, *et al.*, Epitaxial $ZrSe_2$/$MoSe_2$ semiconductor vd Waals heterostructures on wide band gap AlN substrates, *Microelectron. Eng.*, 2015, **147**, 269–272.
61 S. Singh, Z. Zanolli, M. Amsler, B. Belhadji, *et al.*, Low-energy phases of Bi monolayer predicted by structure searching two dimensions, *J. Phys. Chem. Lett.*, 2019, **10**, 7324–7332.
62 K. Mathew, R. Sundararaman, K. Letchworth-Weaver, *et al.*, Implicit solvation model for density-functional study of nanocrystal surfaces and reaction pathways, *J. Chem. Phys.*, 2014, **140**(8), 084106.
63 C. F. Fu, J. Sun, Q. Luo, *et al.*, Intrinsic electric fields in two-dimensional materials boost the solar-to-hydrogen efficiency for photocatalytic water splitting, *Nano Lett.*, 2018, **18**(10), 6312–6317.
64 G. Wang, J. Chang, S. D. Guo, *et al.*, MoSSe/Hf (Zr) S_2 heterostructures used for efficient Z-scheme photocatalytic water-splitting, *Phys. Chem. Chem. Phys.*, 2022, **24**(41), 25287–25297.
65 B. Lu, X. Zheng and Z. Li, Two-dimensional lateral heterostructures of triphosphides: AlP_3–GaP_3 as a promising photocatalyst for water splitting, *ACS Appl. Mater. Interfaces*, 2020, **12**(48), 53731–53738.
66 X. Q. Wan, C. L. Yang, X. H. Li, *et al.*, Insights into photogenerated carrier dynamics and overall water splitting of the CrS_3/GeSe heterostructure, *J. Phys. Chem. Lett.*, 2023, **14**(40), 9126–9135.
67 J. C. Lai, L. Li, D. P. Wang, *et al.*, A rigid and healable polymer cross-linked by weak but abundant Zn (II)-carboxylate interactions, *Nat. Commun.*, 2018, **9**(1), 2725.
68 P. Zhou, I. A. Navid, Y. Ma, *et al.*, Solar-to-hydrogen efficiency of more than 9% in photocatalytic water splitting, *Nature*, 2023, **613**(7942), 66–70.
69 R. Long and O. V. Prezhdo, Quantum coherence facilitates efficient charge separation at a MoS_2/$MoSe_2$ van der Waals junction, *Nano Lett.*, 2016, **16**, 1996–2003.
70 F. Ceballos, M. Z. Bellus, H. Y. Chiu and H. Zhao, Ultrafast charge separation and indirect exciton formation in a MoS_2–$MoSe_2$ van der Waals heterostructure, *ACS Nano*, 2014, **8**, 12717–12724.
71 W. Dou, Y. Jia, X. Hao, Q. Meng, J. Wu, *et al.*, Time-domain *ab initio* insights into the reduced nonradiative electron-hole recombination in $ReSe_2$/MoS_2 van der Waals heterostructure, *J. Phys. Chem. Lett.*, 2021, **12**, 2682–2690.
72 J. He, L. Zhang, D. He, Y. Wang, Z. He and H. Zhao, Ultrafast transient absorption measurements of photocarrier dynamics in monolayer and bulk $ReSe_2$, *Opt. Express*, 2018, **26**, 21501–21509.
73 X. Hong, J. Kim, S. F. Shi, Y. Zhang, C. Jin, Y. Sun, *et al.*, Ultrafast charge transfer in atomically thin MoS_2/WS_2 heterostructures, *Nat. Nanotechnol.*, 2014, **9**, 682–686.
74 Q. Zheng, W. A. Saidi, Y. Xie, Z. Lan, O. V. Prezhdo, *et al.*, Phonon-assisted ultrafast charge transfer at van der Waals heterostructure interface, *Nano Lett.*, 2017, **17**, 6435–6442.
75 Z. Zhang, W. H. Fang and R. Long, *et, al.*, Exciton dissociation and suppressed charge recombination at 2D perovskite edges: key roles of unsaturated halide bonds and thermal disorder, *J. Am. Chem. Soc.*, 2019, **141**, 15557–15566.
76 Y. Wei, W. H. Fang and R. Long, Covalent functionalized black phosphorus greatly inhibits nonradiative charge recombination: a time domain *ab initio* study, *J. Phys. Chem. Lett.*, 2020, **11**, 478–484.
77 J. He, D. Casanova, W. H. Fang, R. Long, *et al.*, MAI termination favors efficient hole extraction and slow charge recombination at the $MAPbI_3$/CuSCN heterojunction, *J. Phys. Chem. Lett.*, 2020, **11**, 4481–4489.
78 S. V. Kilina, A. J. Neukirch, B. F. Habenicht, D. S. Kilin, *et al.*, Quantum zeno effect rationalizes the phonon bottleneck in semiconductor quantum dots, *Phys. Rev. Lett.*, 2013, **110**, 180404.
79 Y. Wang and R. Long, Rapid decoherence induced by light expansion suppresses charge recombination in mixed cation perovskites: time-domain *ab initio* analysis, *J. Phys. Chem. Lett.*, 2020, **11**, 1601–1608.
80 P. Sabatier, *et, al.*, Hydrogénations et déshydrogénations par catalyse, *Chem. Ges.*, 1911, **44**, 1984–2001.
81 J. Rossmeisl, Z. W. Qu, H. Zhu, G. J. Kroes, *et al.*, Electrolysis of water on oxide surfaces, *J. Electroanal. Chem.*, 2007, **607**, 83–89.
82 J. K. Nørskov, J. Rossmeisl, A. Logadottir, *et al.*, Origin of the overpotential for oxygen reduction at a fuel-cell cathode, *J. Phys. Chem. B*, 2004, **108**, 17886–17892.
83 Y. Fan, X. Song, X. Ma, W. Li and M. Zhao, Rational design of black phosphorus-based direct Z-scheme photocatalysts for overall water splitting: The role of defects, *J. Phys. Chem. Lett.*, 2022, **13**, 9363–9371.
84 D. A. Kuznetsov, Z. Chen, P. V. Kumar, *et al.*, Single site cobalt substitution in 2D molybdenum carbide (MXene) enhances catalytic activity in the hydrogen evolution reaction, *J. Am. Chem. Soc.*, 2019, **141**, 17809–17816.

